Three-Dimensional Brain Imaging of Spatiotemporal Changes in Small Animals Using Diffuse Optical Tomography

Ernesto E. Vidal-Rosas[1], Daniel Coca[1], Stephen A. Billings[1], Ying Zheng[2]
John E.W. Mayhew[2], David Johnston[2], Anneurin Kennerly[2]

[1] University of Sheffield, Department of Automatic Control and Systems Engineering, Sheffield S1 3Jd, UK
[2] University of Sheffield, Department of Psychology, Sheffield S10 2TN, UK

Abstract. This paper demonstrates the potential of diffuse optical tomography for estimating the temporal evolution of the haemodynamic response following cortical activation is small animals. In order to improve the spatial resolution and quantitative accuracy, a priori anatomical and functional information, derived from MR scans and prior physiological evidence, is incorporated in the reconstruction algorithm. Results from numerical and experimental studies demonstrate that the approach can effectively recover the location, spatial extent and temporal evolution of the haemodynamic response.

1 Introduction

Non-invasive functional brain imaging of small animals has a major scientific impact in physiology studies where small animals, especially rodents, provide models to investigate haemodynamic changes or metabolism.
Several imaging devices are currently available, such as functional Magnetic resonance imaging (fMRI), Positron Emission Tomography (PET), X-ray Computer Tomography (CT), Single Photon Emission Tomography (SPECT), Ultrasound (US) and, recently, Diffuse Optical Tomography (DOT). Although research in this imaging modality is still ongoing, DOT is emerging as a powerful complementary technique to fMRI. This is, with DOT it is possible to monitor signals that can not be detected by using fMRI; for example, simultaneous monitoring of both oxy- and deoxy-haemoglobin, and this is achieved without requiring external contrast agents, because in DOT, the intrinsic absorption and scattering properties of tissue are exploited [1]
Other important feature in DOT is the high speed of data acquisition, that can be as fast as 0.16 seconds for a complete scan [2]. Other advantages include the relatively lower cost when compared to other modalities such as MRI, the portability and compactness of the equipment and the non-ionizing radiation which is harmless to the human being [3].
In DOT, tissue is illuminated with near-infrared light from an array of sources. The light transmitted or reflected is measured by an array of detectors. The

spatially varying optical parameters of tissue (absorption and scattering) are recovered by solving an ill-posed inverse problem (the number of unknowns that are to be estimated is far grater than the number of measurements), based on a forward model describing the propagation of light transport through tissue [4]. The main disadvantage that prevents DOT to be used routinely as an independent imaging modality is the current limitation of spatial resolution, caused mainly by the strong light scattering in tissue, which produces multiple internal redirections on the incident light, leading to a diffuse process to govern the propagation and thus, generating a random process. Attempts to solve this problem with ordinary algorithms such as ART (Algebraic Reconstruction Technique), SART (Simultaneous Algebraic Reconstruction Technique) [3] and SIRT (Simultaneous Iterative Reconstruction Technique) [5] result in erroneous and inaccurate solutions, and therefore more sophisticated algorithms are required. Several groups have developed imaging procedures to be used in small animals, and important steps have been taken towards improving the spatial resolution [5-8]. In this work, a number of approaches aimed at improving the spatial resolution and quantitative accuracy of DOT are implemented and evaluated using synthetic and real experimental data. Specifically, structural MR scans were used to develop a finite element model of the rat's head, incorporating all relevant anatomical structures. The 3D finite element mesh was parameterized using available information about the optical properties of different types of tissue. The anatomical information combined with existing physiological evidence were used as a priori information in the process of reconstructing the three dimensional maps of absorption at specific time points within a time series. This paper is organized as follows: description of the instrumentation and the underlying theory for DOT imaging is introduced in Sections 2.1-2.4. Section 2.5 describes the incorporation of a priori information. Sections 2.6 and 2.7 describe the synthetic and experimental data sets used in this study. Results from synthetic and real data are presented to in Section 3 to demonstrate the viability of the proposed approach.

2 Methods

2.1 Instrumentation

Different imaging devices have been developed during the last 10 years for studies in small animals using continuous wave systems [5, 6, 9]. In this work, the device used to perform the measurements was the Dynamic Near-Infrared Optical Tomography (DYNOT) instrument marketed by NIRx [10] which operates in continuous mode. The instrument can be divided into three main units: delivery, detection and control. The delivering unit consists of four high power laser diodes at wavelengths 725nm, 760nm, 810nm and 830nm. The source-detector combination is single-source-parallel-detection; therefore the light is firstly focused into an optical de-multiplexer. Light is delivered into the medium through bifurcated fiber bundles which consist of a fine fiber of 3mm immerse into a wider fiber of 7mm. With this feature, delivery and collection of light can be performed at

the same place. The nominal output power of the laser light is 400mW which is reduced to 100mW due to the de-multiplexer. Finally around 30mW reaches the target. In the detection unit, the detectors are silicon photodiodes. They provide high dynamic range and high linearity, although the detection response is slow and they are temperature dependent. Parallel detection is obtained by a lock-in technique. Laser sources are intensity modulated at different frequencies and then, lock-in amplifiers fed by the signal from the detectors remove the DC offsets, the room light and simultaneously distinguish the different wavelengths. A set of amplifiers, before and after the lock-in detection, improve the signal-to-noise ratio and perform the signal conditioning for data acquisition. The device can acquire 32 parallel signals at four different wavelengths. The acquisition rate is 3Hz with a dynamic range of 180dB. The device is operated using a virtual control panel developed in LabVIEW (National Instruments) which provides calibration and data display, other features include procedures to evaluate the performance of the device.

2.2 Modelling of Light in Tissue

The main stages involved in the reconstruction process are: modelling of light transport in tissue, forward problem and inverse problem. Most of the implementations in describing the transport of light in tissue are based on the Radiative Transport Equation (RTE) which is an energy balance equation. According to transport theory, the radiance ϕ ($\mathrm{W\,m^{-2}sr^{-1}}$) of light at position r travelling in a direction of the unit vector $\hat{s}$ is decreased by absorption and scattering but it is increased by light that is scattered from $\hat{s}'$ direction into direction $\hat{s}$ [11]:

$$\left(\frac{1}{c}\frac{\partial}{\partial t} + \hat{s}\cdot\nabla + \mu_{tr}\left(r\right)\right)\phi\left(r,\hat{s},t\right) = \mu_s \int_{S^{n-1}} \Theta\left(\hat{s}\cdot\hat{s}'\right)\phi\left(r,\hat{s},t\right)d\hat{s}' + q\left(r,\hat{s},t\right) \tag{1}$$

where $\mu_{tr} = \mu_a + \mu_s$ is the total attenuation coefficient, $d\hat{s}'$ is the differential solid angle in the direction $\hat{s}$ and $\Theta(\hat{s}\cdot\hat{s}')$ is the scatter phase function, which gives the probability of a photon scattering from direction $\hat{s}$ to $\hat{s}'$. The form of the scattering function is unknown, but usually it is characterized by a single parameter g called average cosine of the phase function. This parameter is a measure of the asymmetry of the single scattering pattern; for instance, g with values 1, 0 and -1 describes extremely forward, isotropic and highly backward scattering, respectively. According to the literature [12], the typical values for near-infrared (NIR) wavelengths are $0.75< \mu_a < 0.99$.
Because of the difficulty in solving the RTE equation exactly, several approximations have been proposed. The most common is the P_N approximation which is obtained by the spherical harmonics expansion of equation (1). The approximation gives rise to a system of $(N+1)^2$ first -order partial differential equations. Using this approach, high values of N should be considered in order to approximate the exact solution, which ideally is an infinite sum of Legendre polynomials [13]. The simplest form is the P_1 approximation in which the infinite sum of polynomials is truncated to the first two terms. A further reduction from the P_1

approximation is the Diffusion Equation (DE) which is by far the most widely used model to describe the light transport in tissue. For the continuous mode, this equation is independent on time and is given by

$$-\nabla \cdot D\left(\mathbf{r}\right)\nabla\phi\left(\mathbf{r}\right)+\mu_a\left(\mathbf{r}\right)\phi\left(\mathbf{r}\right)=q\left(\mathbf{r}\right) \tag{2}$$

where $D=1/3(\mu_a+\mu_s')$. This parameter is known as the diffusion coefficient and it quantifies the scattering properties of the material, q is an isotropic source, $\mu_s'=(1-g)\mu_s$ is the reduced scattering coefficient and $\phi(\mathbf{r})$ is the photon density at $\mathbf{r}$. The boundary condition at tissue surface is modelled by a Robin Boundary Condition (RBC)

$$\phi\left(\xi\right)+2AD\left(\xi\right)\frac{\partial\phi\left(\xi\right)}{\partial\boldsymbol{n}}=0 \tag{3}$$

where $\boldsymbol{n}$ is a normal vector to the surface $\partial\Omega$, $\xi\in\partial\Omega$ and A is a factor that takes into account the refractive index mismatch between air and tissue. The outward current, which is the quantity measured by detectors, is calculated from

$$\Gamma\left(\xi\right)=-D\left(\xi\right)\boldsymbol{n}\cdot\nabla\phi\left(\xi\right)\,. \tag{4}$$

2.3 Forward Problem

In this stage of the reconstruction process, the transport of light in a scattering medium is calculated by considering the medium properties and its interactions with the surroundings. The DE was selected to solve the forward problem, because of the accuracy in representing the propagation of light and its simplicity which allows finding the solution faster than Monte Carlo methods or the RTE. The DE was solved numerically using the Finite Element Method (FEM). Following the variational formulation in three-dimensions for the time-independent diffusion equation (2), the solution is obtained by minimizing the so called first functional given by

$$\delta F\left(\phi\right) \tag{5}$$

where

$$F\left(\phi\right)=\tfrac{1}{2}\iiint\limits_{\Omega}\left[D\left(\mathbf{r}\right)_x\left(\tfrac{\partial\phi}{\partial x}\right)^2+D\left(\mathbf{r}\right)_y\left(\tfrac{\partial\phi}{\partial y}\right)^2+D\left(\mathbf{r}\right)_z\left(\tfrac{\partial\phi}{\partial z}\right)^2+\mu_a\phi^2\right]d\Omega+ A\iiint\limits_{\partial\Omega}D\left(\xi\right)\phi^2 d\partial\Omega-\iiint\limits_{\Omega}f\phi d\Omega\,. \tag{6}$$

However, last equation considers all the values in a continuous space. In order to apply the FEM, the functional $F(\phi)$ is approximated by a sum of subfunctionals, one for each element

$$F\left(\phi\right)=\sum_{e=1}^{M_e}F^e\left(\phi^e\right)+\sum_{s=1}^{M_s}F^s\left(\phi^s\right) \tag{7}$$

where M_e represents the number of solid elements and M_s the number of surface elements. Furthermore, the unknown function is approximated by a sum of

polynomial functions within each solid element by

$$\phi^e(x,y,z) = \sum_{j=1}^{n_e} N_j^e(x,y,z)\,\phi_j \tag{8}$$

where n_e is the number of nodes in a solid element, similarly, for each surface element by

$$\phi^s(x,y,z) = \sum_{j=1}^{n_s} N_j^s(x,y,z)\,\phi_j \tag{9}$$

where n_s is the number of nodes in a surface element. After taking the partial derivatives of the functional F with respect to ϕ and by imposing the stationary requirement on F, according to the variational formulation, equation (6) is reduced to

$$\sum_{i,j=1}^{n_e} \phi_j^e \iiint_\Omega \left(D(\mathbf{r})_x \frac{\partial N_i^e}{\partial x}\frac{\partial N_j^e}{\partial x} + D(\mathbf{r})_y \frac{\partial N_i^e}{\partial y}\frac{\partial N_j^e}{\partial y} + D(\mathbf{r})_z \frac{\partial N_i^e}{\partial z}\frac{\partial N_j^e}{\partial z} + \mu_a(\mathbf{r}) N_i^e N_j^e \right) d\Omega$$
$$- \iiint_\Omega q N_i^e d\Omega + 2A \sum_{i,j=1}^{n_s} \phi_j^s \iint_{\partial\Omega} D(\xi) N_i^s N_j^s d\partial\Omega = 0\,. \tag{10}$$

This result can be expressed in matrix form as

$$[\mathbf{K}(D) + \mathbf{C}(\mu_a) + \mathbf{F}]\,\phi = \mathbf{Q} \tag{11}$$

where

$$\begin{aligned}
K_{ij} &= \iiint_\Omega \left(D(\mathbf{r})_x \frac{\partial N_i^e}{\partial x}\frac{\partial N_j^e}{\partial x} + D(\mathbf{r})_y \frac{\partial N_i^e}{\partial y}\frac{\partial N_j^e}{\partial y} + D(\mathbf{r})_z \frac{\partial N_i^e}{\partial z}\frac{\partial N_j^e}{\partial z} \right) d\Omega \\
C_{ij} &= \iiint_\Omega \mu_a(\mathbf{r}) N_i^e N_j^e d\Omega \\
F_{ij} &= 2A \iint_{\partial\Omega} D(\xi) N_i^s N_j^s d\partial\Omega \\
Q_{ij} &= \iiint_\Omega q N_i^e d\Omega\,.
\end{aligned} \tag{12}$$

The polynomial functions N^e and N^s used to discretize the space Ω were piecewise linear basis function, corresponding to tetrahedral and triangular elements, respectively. After performing the assembly process, calculation of ϕ is straightforward by using sparse matrix solvers.

2.4 Inverse Problem

In DOT, the forward problem can be stated as: given the spatial distribution of the medium properties and the distribution of the sources delivering light on it, find the resulting measurements at the surface; and the inverse problem: given

the distribution of the sources and the measurements on the surface, find the spatial distribution of properties of the medium. In order to solve the inverse problem, a long-established approach in optical tomography is to state the inverse problem as a linear perturbation equation. This formulation, in continuous-wave systems, consists of relating two sets of differences [3]:

1. The difference between measurements taken by the optodes (u) and the measurements predicted by a model (u_s):

$$\delta\mathbf{u} = \mathbf{u} - \mathbf{u}_s \,. \tag{13}$$

2. The difference between the (unknown) optical properties of the target medium and the optical properties of a reference medium used to generate the predicted measurements u_s. This difference is represented by the set $\delta\mathbf{x}$.

The relation is stated in the following formula:

$$\mathbf{W}_s\delta\mathbf{x} = \delta\mathbf{u} \tag{14}$$

where $\mathbf{W}_s$ is the sensitivity matrix given by the Jacobian, and represents the effect that a perturbation in the optical properties in the medium have on the calculated measurements. Inversion of matrix $\mathbf{W}_s$ is the basis for image reconstruction; however, the reliability on the obtained solution $\delta\mathbf{x}$ is influenced by several factors including measurement errors, uncertainty on the optical parameters of tissue and the inaccuracy of the model. To minimize these factors, the Normalized Difference Method (NDM) was employed [14]. This method evaluates relative measurements and consists of measuring the change or changes of the outward flux between two states, called the reference state and the perturbed state. For the case considered in here, these states belong to a time series, in which case the aim is to recover the complete dynamic of changes [15]. The inverse formulation using the NDM is

$$\mathbf{W}_s\delta\mathbf{x} = \left[\frac{(\mathbf{u}_1)_i - (\mathbf{u}_2)_i}{(\mathbf{u}_2)_i}\right](\mathbf{u}_s)_i \tag{15}$$

where $(\mathbf{u}_1)_i$ represent the outward flux recorded at a specific time point, $(\mathbf{u}_2)_i$ the time-averaged outward flux, both acquired from the ith source-detector pair.$\mathbf{W}_s$ and $\delta\mathbf{x}$ are the same as before.
The inverse problem was solved using an iterative approach and this consists of three main components:

1. A model that describes the propagation of light in tissue.
2. The sensitivity calculation of each source-detector pair to changes in the optical properties of the medium. Specifically in this work, the aim is to reconstruct changes in the absorption parameter.
3. A method to up-date the previous solution.

The model was previously described and the Jacobian was calculated from reciprocity theorem from the radiative transfer theory [13], which in the context of

DOT, it states that the flux perceived by a detector from a source located at a specific point in the space, is equal to the photon density at that point due to a source located at the detector position. This new source, called the adjoint source, and the second part of the theorem lead to the adjoint diffusion equation represented by

$$\begin{gathered} -\nabla \cdot D\left(\mathbf{r}\right) \nabla \phi_{adj}\left(\mathbf{r}\right) + \mu_a\left(\mathbf{r}\right) \phi_{adj}\left(\mathbf{r}\right) = 0 \\ \phi_{adj}\left(\xi\right) + 2AD\left(\xi\right) \frac{\partial \phi_{adj}(\xi)}{\partial v} = q^*\left(\xi\right) \quad \xi \in \partial\Omega \end{gathered} \tag{16}$$

where $q*$ is the adjoint source defined on the boundary at detector position. To calculate the Jacobian, equation (16) must be solved for ϕ_{adj} and then, in the finite element framework, the Jacobian for absorption changes at position is calculated from

$$\mathbf{W}_s = J_{\mu_a}\left(\xi_j, \zeta_i, \mathbf{r}\right) = \left[\sum_{k|N_k \in \tau(\mathbf{r})} \phi_k^{(i)}\left(\mathbf{r}\right) N_k\left(\mathbf{r}\right)\right] \times \left[\sum_{k|N_k \in \tau(\mathbf{r})} \phi_{adj,k}^{(j)}\left(\mathbf{r}\right) N_k\left(\mathbf{r}\right)\right] \tag{17}$$

for a source at position ζ_i and an adjoint source at detector position ξ_j. N_k is the polynomial function used to discretize the domain Ω and τ is the element containing the point $\mathbf{r}$ [16]. The form of matrix (17) leads to a poorly conditioned linear system and pre-conditioning of this sensitivity matrix is required. The approach taken in this work is the matrix rescaling technique which also provides more sensitivity at the interior of the medium, rather than at the boundaries, which is a characteristic of the Jacobian J_{μ_a} for the type of measurements obtained using continuous-wave systems [17].
Finally, the perturbation $\delta\mathbf{x}$ is obtained by seeking a the least-square solution of equation (15), this is, by minimizing the squared error E given by

$$E = \frac{1}{2}\left(\mathbf{W}_s\delta\mathbf{x} - \delta\hat{\mathbf{u}}\right)^{\mathrm{T}}\left(\mathbf{W}_s\delta\mathbf{x} - \delta\hat{\mathbf{u}}\right) = \frac{1}{2}\delta\mathbf{x}^{\mathrm{T}}\cdot\mathbf{A}\cdot\delta\mathbf{x} - \mathbf{b}^{\mathrm{T}}\cdot\delta\mathbf{x} + \frac{1}{2}\left(\delta\hat{\mathbf{u}}\right)^{\mathrm{T}}\cdot\left(\delta\hat{\mathbf{u}}\right) \tag{18}$$

where $\delta\hat{\mathbf{u}} = (\mathbf{u}_s)_i[(\mathbf{u}_1)_i - (\mathbf{u}_2)_i]/(\mathbf{u}_2)_i$, $\mathbf{A} = \mathbf{W}_s^{\mathrm{T}} \cdot \mathbf{W}_s$ and $\mathbf{b} = \mathbf{W}_s^{\mathrm{T}} \cdot \delta\mathbf{u}$. Setting to zero the derivative of E with respect to the unknown, it results in

$$\frac{\partial E}{\partial\left(\delta\mathbf{x}\right)} = \mathbf{A}\cdot\delta\mathbf{x} - \mathbf{b} = 0\,. \tag{19}$$

The conjugate gradient descendent method was used to solve iteratively equation (19) and this can be found elsewhere [18].

2.5 Anatomical and Functional a Priori Information

DOT provides high temporal resolution when compared with other modalities such as MRI. Conversely, the spatial resolution of DOT is inferior to MRI. The reason is the high scattering coefficient in most of biological tissues, which means that light can only travel a few millimetres inside tissue before it is effectively

scattered. Therefore, a diffuse process dominates light propagation, blurring the spatial information and consequently the images obtained. One effective way of improving the spatial accuracy is by providing a priori information regarding anatomy or physiology of tissue. Usually, structural information is provided to the reconstruction process in terms of anatomical maps derived, for example, from MRI scans [19]. This information is included in the forward model, leading to more realistic simulations and then improving the image reconstruction.
In small animals studies, a priori anatomical information has been obtained from rat cranium cryo-sections [7] and from MRI images [8]. The latter has the disadvantage that anatomical maps are rescaled to fit the size and shape of individuals, while the former does not suffer from this systematic error because the animal can be scanned before experiment and furthermore, concurrent measurements can be obtained if MRI and DOT are coupled, which is known as multimodal dynamic imaging [20].
In this work, pixel images were acquired from a 7-T high field animal magnet (Bruker BioSpin). Each image was segmented into skin, skull, muscle and brain using image processing techniques and then all the slices were stacked together to build a three-dimensional model of the rat's head, which later was converted into a finite element mesh which consisted of 8553 nodes and 40883 elements. These steps were accomplished using Scan IP & Scan FE [21] and the process is illustrated in Fig. 1.
Based on values taken from literature, typical optical parameters at 800-nm

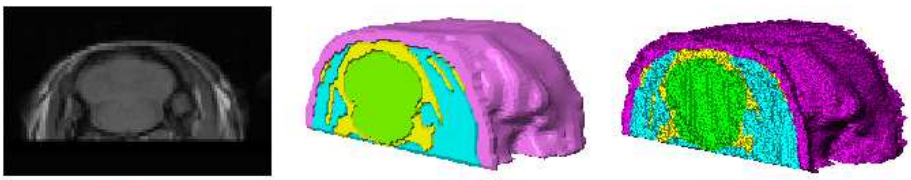

Fig. 1. 3D image modelling: (a) Acquisition of raw data, (b) voxelization and smoothing of processed data and (c) FEM mesh.

light were assigned to the node locations of the different tissues considered. The absorption coefficients assigned were $\mu_a = 0.02\,\mathrm{mm}^{-1}$ for skin, $0.005\,\mathrm{mm}^{-1}$ for skull, $0.015\,\mathrm{mm}^{-1}$ for brain and $0.022\,\mathrm{mm}^{-1}$ for muscle. The corresponding scattering coefficients were $0.5\,\mathrm{mm}^{-1}$ for skin, $1.63\,\mathrm{mm}^{-1}$ for skull, $1.63\,\mathrm{mm}^{-1}$ for brain and $1\,\mathrm{mm}^{-1}$ for muscle [7].
Spatial a priori information can also be incorporated in the solution of the inverse problem by providing location of the activation area; this is, by constraining the location of perturbations to lie in the cortex. A straightforward way of accomplishing this is by assuming $\delta\mathbf{x} = 0$ for all nodes which location is outside the activation area, thus reducing considerably the number of unknowns and

implicitly the computational cost. It has been proved that this simple concept significantly improves image reconstruction results, in magnitude and location of perturbations [19, 22]. In addition, functional a priori information can be included in the inverse solution by imposing positivity and negativity constraints to the direction of the perturbation, based on physiological evidence. Previous works reported improvement in image quality, such as the reduction of artefacts due to the sources [23] or the significant increase of internal detail [18].
In this work, the left whisker pad was stimulated and the corresponding spatial constraint was applied, additionally, physiologic evidence suggests that whisker stimulation enlarge blood supply and hence increasing oxygen absorption [24], this functional information was included in the solution of the inverse problem by imposing a positivity constraint in the iterative algorithm.

2.6 Simulation of Spatiotemporal Changes in the Brain

To test the viability of the reconstruction framework described previously, simulated experiments were performed. A target medium is shown in Fig. 3 and it consists of a three-dimensional finite element mesh of the rat's head with an embedded absorber in the left hemisphere. Probes were fixed in a honeycomb structure formed by a plate with 12 optodes, with each optode working as a source and as a detector resulting in 144 source-detector pairs. The center-to-center distance between neighbouring probes is 4.2mm and the selected geometry follows results indicating that the best probe array to reduce image blurring is a hexagonal geometry [25].
Background properties of the medium are the same as before, while a time

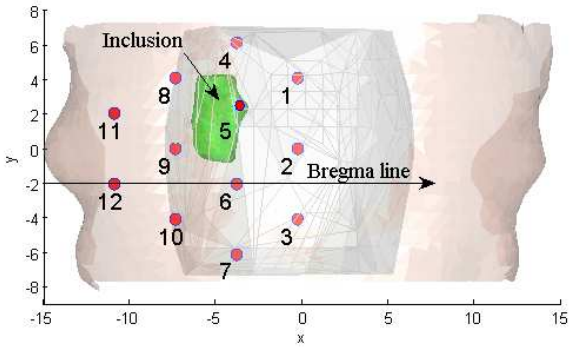

Fig. 2. Location of inclusion inside the brain of the rat and positioning of honeycomb structure on the top of the head.

varying function $\mu_a(\mathbf{r}, t)$ was assigned to the optical properties of the inclusion. Previous works reported dynamic reconstructions in two-dimensions using time-varying functions related to vascular activity including quasi-periodic, chaotic

and stochastic signals [14, 15]. A quasi-periodic signal was assigned to the inclusion, generated by adding to sinusoidal functions with incommensurable frequencies given by $q_n(\mathbf{r}, t) = [\cos(\pi/8)\, n + \sin(\sqrt{\pi}/4)\, n]/2$ [14].
Synthetic measurements were calculated by solving the forward problem for each time-point in the series; however, before solving the inverse problem, some caution actions were taken to avoid inverse crime [26]. Firstly, 1% of Gaussian noise was added to the background optical properties before calculating the detector measurements to account for heterogeneity in tissue. Secondly, different meshes were used to generate synthetic data and to solve the forward model implemented within the inverse solver; that is, the mesh used in the reconstruction process was obtained after randomizing the mesh used to generate synthetic data, by adding 3% of noise to the nodes locations. Other option is to derive measurements from a mesh with higher resolution [27]; however, for the relative measurements taken in this work, this strategy does not have a marked effect on the synthetic data. Finally, 3% of Gaussian distributed random noise was added to measurements. These last actions accounted for the structure mismatch between 'real' and simulated experiments and for noise level.

2.7 Experimental Setup

Small animals provide excellent models to investigate ischemia [7], tissue oxygenation [9] and haemodynamics [28-30]. This work focuses on somatosensory cortex stimulation, and specifically, on the rodent barrel cortex, a well known model to investigate neural activity and cerebral blood flow.
The animals used were female Hooded Lister rats weighing between 250 to 400 g, kept in a 12 h dark/light cycle environment and constant temperature of 22 °C with food and water ad libitum. The rat was anaesthetized with urethane (1.25 g/kg i.p.) and atropine (0.1 ml) was administrated to reduce mucous secretions during surgery. Rectal temperature was maintained at 37 °C through the surgical and experimental procedures by means of a homoeothermic blanket (Harvard apparatus). The animal was tracheotomized to allow artificial ventilation. Ventilation parameters were adjusted to maintain blood gas measurements within physiological limits. Measurement of mean arterial blood pressure was performed after the left and right femoral veins were cannulated, in this stage, Phenylephrine (0.13-0.26 mg/hr) was infused to keep blood pressure between physiological limits (MABP, 100-110 mmHg).
The left whisker pad was stimulated with tungsten electrodes, which were inserted in the posterior direction between rows A/B and C/D, ensuring that the entire whisker pad was activated following the electrical stimulus. The electrical stimulus consisted of a 16 seconds, 1.6mA current pulse, and 96 seconds of Inter-Stimulus Intervals (ISI). The intensity gives a large haemodynamics response, but does not affect blood pressure or heart rate [31]. Once the surgery was finished, the animal was placed in a nonmagnetic platform in prone position, fixed via two ear bars and a bite bar. The honeycomb structure was adjusted such that source nine was positioned on the rodent barrel cortex; this is, at the 2 mm back the Bregma line.

3 Results

3.1 Reconstruction of Spatiotemporal Changes in the Brain

Reconstruction of spatiotemporal changes implies the evaluation of two features: the location of obtained volumetric perturbation and the information given by the complete reconstructed time series. Location of the inclusion for t=0 s is shown in Fig. 3a, and its corresponding reconstructed image is displayed in Fig. 3b. Solution are limited to 200 iteration, further this point, no improvement was obtained in the image. Although it was not possible to recover the exact shape of the perturbation, its location is precise, enclosed in the brain as it was expected.

In order to compare the temporal variation of the reconstructed volumetric

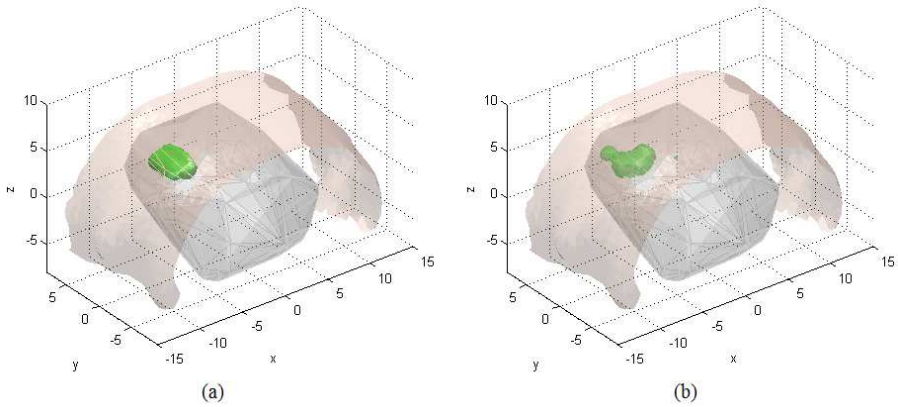

Fig. 3. (a) Original inclusion within the brain. (b) Reconstructed change also constrained within the brain

images for all the time series, a similar procedure as in Pei [14] was followed. Specifically, in order to compare the recovered time series with the original temporal variation, a pseudo-state-space (PSS) trajectory was generated for each signal. A single node with coordinates was selected within the reconstructed volumetric image. Its temporal variation is show in the upper plot in Fig. 4b. Also, in the lower plot of the same panel, the PSS trajectory is displayed. Comparison with the original functional perturbation (Fig. 4a) reveals a remarkably concordance between the two time series.

The effect of applying spatial and sign constraints on the quality of reconstruction are illustrated in Fig. 5. With no spatial constraints, the CGD algorithm leads to an incorrect solution (Fig. 5a) in which the inclusion is located in the skull and skin rather than in the brain. In Fig. 5b, a reconstructed image is shown after imposing only spatial constraints. In this case, positive and negative changes are obtained, when originally only positive changes were simulated.

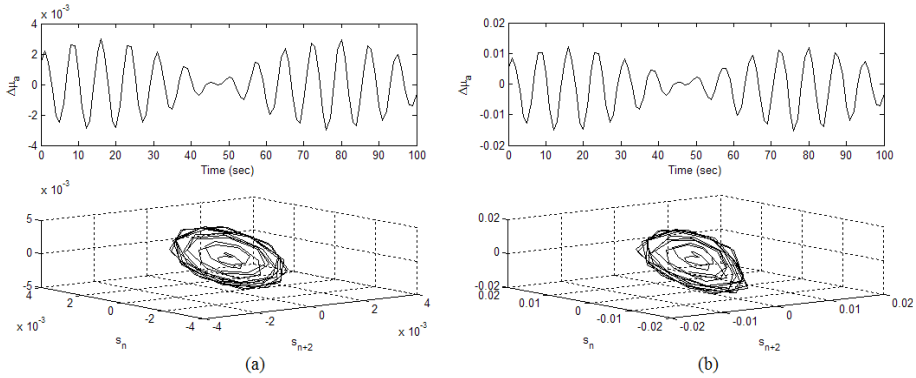

Fig. 4. (a) Upper plot shows the temporal variation of the inclusion and lower plot is the PSS trajectory. (b) Upper plot is the temporal variation of a selected node within the reconstructed volumetric image and the lower plot is the PSS trajectory.

Combination of both constraints clearly improves the location and the right direction of the perturbation, as it can be seen in Fig. 5c.Reconstructions shown in Fig. 5 were limited to 200 iterations. However, for the second case, in which sign constraints were missed (Fig 5b), the CGD algorithm continued improving the solution and after 500 iterations, a reconstructed perturbation with the right direction dominated the image.

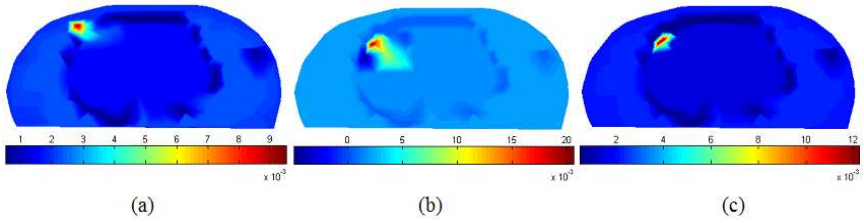

Fig. 5. Effect that spatial and sign constraints have on reconstruction. (a) Only sign constraints were imposed to the CGD algorithm. (b) Only spatial a priori information was included in the reconstruction. (c) Combination of sign and spatial constraints imposed to the CGD algorithm

3.2 Reconstruction Induced Haemodynamic Changes due to Whisker Pad Stimulation

To evaluate the performance of the combined techniques, reconstructed images were obtained from haemodynamics changes in the rat's brain due to so-

matosensory stimulation. Measurement of absorption changes were done with the DYNOT instrument. Data set for each wavelength was averaged through seven trials, and then the Normalized Difference Method [14] was used to deal with the relative changes obtained from differential measurements taken. The profile of the processed signal at λ=760nm is displayed in Fig. 6a. The wide line is the mean of the 144 source-detector pairs. The stimulus started at t=0 s and continued until t=16 s. It can be seen a markedly active state, with the haemodynamic response prolonged several seconds after the end of the stimulus. Also, the V-signal, with a frequency of 0.1 Hz, appears visible all through the experiment.
Reconstruction for t=16 s is displayed in Fig. 6b. Convergence was achieved after 200 iterations. Spatial extent of the haemodynamic reconstructed change is correct in size, but its location is 1 mm far from the expected location [32]. This can be explained by a mismatch between the modelled source and the real location. However, the result is within the precision obtained with diffusive light measurements [33].

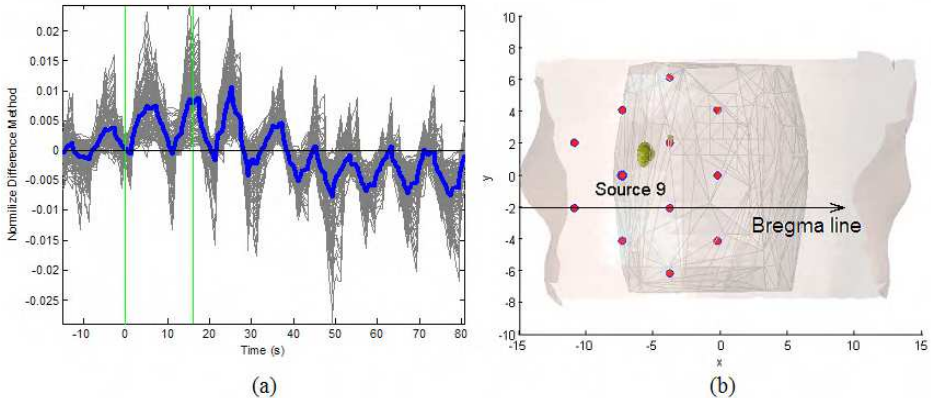

Fig. 6. (a)Measurements profile by applying the Normalized Difference Method (NDM), (b)Reconstructed image showing the activation area, accurate in spatial extent and location

Conclusions

Recovered images, using synthetic or simulated data, offer good insight about performance of the combined strategies taken through the reconstruction process. Dynamic changes in the absorption coefficient were successfully recovered in location and relative magnitude, by employing a combination of spatial and direction constraints embedded in the CGD method. The strategies taken improve the ill-conditioning of the inverse formulation, leading to faster convergence and more accurate reconstructions.

Acknowledgements

Authors acknowledge the support from the UK Engineering and Physical Sciences Research Council. E. E. Vidal-Rosas gratefully acknowledges the support from a grant of the National Research Council for Science and Technology (CONACYT).

References

1. Cerussi, A.E., Berger, A.J., Bevilacqua, F., Shah, N., Jakubowski, D., Butler, J., Holcombe, R.F., Tromberg, B.J.: Sources of absorption and scattering contrast for near-infrared optical mammography. Acad. Rad. 8(3), 211-218 (2001)
2. Franceschini, M.A., Toronov, V., Filiaci, M.E., Gratton, E., S. Fantini: On-line optical imaging of the human brain with 160-ms temporal resolution. Opt. Exp. 6(3), 49-57 (2000)
3. Barbour, R.L., Graber, H.L., Chang, J.W., Barbour, S.L.S., Koo, P.C., Aronson, R.:MRI-guided optical tomography: Prospects and computation for a new imaging method. IEEE Comp. Sc. & Eng. 2(4), 63-77 (1995)
4. Arridge, S.R.: Optical tomography in medical imaging. Inv. Prob. 15(2), R41-R93 (1999)
5. Siegel, A.M., Marota, J.J.A., Boas, D.A.: Design and evaluation of a continuous-wave diffuse optical tomography system. Opt. Exp. 4(8), 287-298 (1999)
6. Schmitz, C.H., Graber, H.L., Pei, Y.L., Farber, M., Stewart, M. , Levina, R.D., Levin, M.B., Xu, Y., Barbour, R.L.: Dynamic studies of small animals with a four-color diffuse optical tomography imager. Rev. Sci. Inst. 76(9) (2005)
7. Bluestone, A.Y., Stewart, M., Lasker, J., Abdoulaev, G.S., Hielscher, A.H.: Three-dimensional optical tomographic brain imaging in small animals, part 1: hypercapnia. J. Biomed. Opt. 9(5), 1046-1062 (2004)
8. Pogue, B.W., Paulsen, K.D.: High-resolution near-infrared tomographic imaging simulations of the rat cranium by use of apriori magnetic resonance imaging structural information. Opt. Lett. 23(21), 1716-1718 (1998)
9. Dunn, A.K., Devor, A., Dale, A.M., Boas, D.A.: Spatial extent of oxygen metabolism and hemodynamic changes during functional activation of the rat somatosensory cortex. Neuroimage 27(2), 279-290 (2005)
10. NIRx: DYNOT Imaging System, user manual, http://www.nirx.net/
11. Chandrasekhar, S.: Radiative transfer: Dover Publications. New York (1960)
12. Hielscher, A.H., Bluestone, A.Y., Abdoulaev, G.S., Klose, A.D., Lasker, J., Stewart, M., Netz, U., Beuthan, J.: Near-infrared diffuse optical tomography. Dis. Mar. 18(5-6), 313-337 (2002)
13. Davison, B.: Neutron transport theory: Oxford University Press. Oxford (1957)
14. Pei, Y.L., Graber, H.L., Barbour, R.L.: Influence of systematic errors in reference states on image quality and on stability of derived information for dc optical imaging. App. Opt. 40(31), 5755-5769 (2001)
15. Graber, H.L., Pei, Y.L., Barbour, R.L.: Imaging of spatiotemporal coincident states by DC optical tomography. IEEE Trans. Med. Img. 21(8), 852-866 (2002)
16. Arridge, S.R., Schweiger, M.: Photon-Measurement Density-Functions .2. Finite-Element-Method Calculations. App. Opt. 34(34), 8026-8037 (1995)
17. Arridge, S.R.: Photon-Measurement Density-Functions .1. Analytical Forms. App. Opt. 34(31), 7395-7409 (1995)

18. Pei, Y.L., Graber, H.L., Barbour, R.L.: Normalized-constraint algorithm for minimizing inter-parameter crosstalk in DC optical tomography. Opt. Exp. 9(2), 97-109 (2001)
19. Boas, D.A., Dale, A.M., Franceschini, M.A.: Diffuse optical imaging of brain activation: approaches to optimizing image sensitivity, resolution, and accuracy. Neuroimage 23, S275-S288 (2004)
20. Unlu, M.B., Lin, Y., Birgul, O., Nalcioglu, O., Gulsen, G.: Simultaneous in vivo dynamic magnetic resonance-diffuse optical tomography for small animal imaging. J. Biomed Opt. 13(6), 060501 (2008)
21. Simpleware: ScanIP & ScanFE, http://www.simpleware.com/
22. Ntziachristos, V., Yodh, A.G., Schnall, M.D., Chance, B.: MRI-guided diffuse optical spectroscopy of malignant and benign breast lesions. Neoplasia 4(4), 347-354 (2002)
23. Pogue, B.W., Patterson, M.S., Jiang, H., Paulsen, K.D.: Initial Assessment of a Simple System for Frequency-Domain Diffuse Optical Tomography. Phys. Med. Bio. 40(10), 1709-1729 (1995)
24. Patel, U.: Non-Random Distribution of Blood-Vessels in the Posterior Region of the Rat Somatosensory Cortex. Brain Res. 289(1-2), 65-70 (1983)
25. Boas, D.A., Chen, K., Grebert, ,D., Franceschini, M.A.: Improving the diffuse optical imaging spatial resolution of the cerebral hemodynamic response to brain activation in humans. Opt. Let. 29(13), 1506-1508 (2004)
26. Kaipio, J., Somersalo, E.: Statistical and computational inverse problems: Springer. New York, (2004)
27. Paulsen, K.D., Jiang, H.B.: Spatially Varying Optical Property Reconstruction Using a Finite-Element Diffusion Equation Approximation. Med. Phys. 22(6), 691-701 (1995)
28. Culver, J.P., Siegel, A.M., Franceschini, M.A., Mandeville, J.B., Boas, D.A.: Evidence that cerebral blood volume can provide brain activation maps with better spatial resolution than deoxygenated hemoglobin. Neuroimage 27(4), 947-959 (2005)
29. Culver, J.P., Siegel, A.M., Stott, J.J., Boas, D.A.: Volumetric diffuse optical tomography of brain activity. Opt. Let. 28(21), 2061-2063 (2003)
30. Siegel, A.M., Culver, J.P., Mandeville, J.B., Boas, D.A.: Temporal comparison of functional brain imaging with diffuse optical tomography and fMRI during rat forepaw stimulation. Physics in Medicine and Biology 48(10), 1391-1403 (2003)
31. Kennerley, A.J., Investigation of the haemodynamic response: fMRI techniques with concurrent optical measurements of cerebral blood flow of volume, in Department of Psychology. University of Sheffield: Sheffield. 239 (2006)
32. Fox, K.: Barrel cortex: Cambridge University Press. Camdridge, U.K. (2008)
33. Gibson, A.P., Hebden, J.C., Riley, J., Everdell, N., Schweiger, M., Arridge, S.R., Delpy, D.T.: Linear and nonlinear reconstruction for optical tomography of phantoms with nonscattering regions. App. Opt. 44(19), 3925-3936 (2005)